A 2D Covalent Organic Framework with 4.7-nm Pores and Insight into its Interlayer Stacking

ERIC L. SPITLER,[1] BRIAN T. KOO,[2] JENNIFER L. NOVOTNEY,[1]
JOHN W. COLSON,[1] FERNANDO J. URIBE-ROMO,[1] GREGORY D. GUTIERREZ,[1]
PAULETTE CLANCY,[2]* & WILLIAM R. DICHTEL[1]*

[1]*Department of Chemistry and Chemical Biology,*
[2]*School of Chemical and Biomolecular Engineering,*
Cornell University, Ithaca, New York, 14853 USA

Supporting Information

Correspondence Address

Professor William R Dichtel
Department of Chemistry and Chemical Biology
Cornell University
Baker Laboratory
Ithaca, NY 14853-1301 (USA)
Tel: (+1)-607-254-2356
Fax: (+1)-607-255-4137
Email: wdichtel@cornell.edu

Table of Contents

A. Materials. All reagents were purchased from commercial sources and used without further purification. Mesitylene and dioxane were purchased from commercial sources and used without further purification. Other solvents were purchased from commercial sources and purified using a custom-built alumina-column based solvent purification system.

Instrumentation.

Infrared spectra were recorded on a Thermo Nicolet iS10 with a diamond ATR attachment and are uncorrected.

UV/Vis absorbance spectra were recorded on a Cary 5000 UV-Vis-NIR spectrophotometer with a mercury lamp in either dichloromethane solution or as solids using a praying mantis diffuse reflectance accessory. Emission and excitation spectra were recorded on a Horiba Jobin Yvon Fluorolog-3 fluorescence spectrophotometer equipped with a 450 W Xe lamp, double excitation and double emission monochromators, a digital photon-counting photomultiplier and a secondary InGaAs detector for the NIR range. Correction for variations in lamp intensity over time and wavelength was achieved with a solid-state silicon photodiode as the reference. The spectra were further corrected for variations in photomultiplier response over wavelength and for the path difference between the sample and the reference by multiplication with emission correction curves generated on the instrument. Solid samples were mounted between quartz slides and mounted on a solid sample holder, and emission was observed using a front face detection accessory.

X-ray diffraction patterns were recorded on a Rigaku Smartlab Powder X-Ray Diffractometer in 2θ medium resolution parallel beam/PSA mode employing Cu Kα line focused radiation at 40 kV, 44 mA power and equipped with a Ge crystal detector fitted with a 1.0 mm radiation entrance slit. Samples were mounted on zero background sample holders by dropping powders from a wide-blade spatula and then leveling the sample surface with a glass microscope slide. No sample grinding or sieving was used prior to analysis. Samples were observed using a 0.045º 2θ step scan from 1.0 – 34º (Omega = 1.0º) with an exposure time of 0.4 s per step. No peaks could be resolved from the baseline for $2\theta > 34$º data and was therefore not considered for further analysis.

Thermogravimetric analysis from 20-600 °C was carried out on a TA Instruments Q500 Thermogravimetric Analyzer in nitrogen atmosphere using a 10 °C/min ramp without equilibration delay.

Scanning electron microscopy (SEM) was performed on a FEI Strata 400 FE-SEM. Materials were deposited onto a sticky carbon surface on a flat aluminum platform sample holder. No metal sputtering of the sample was necessary. Focused ion beam (FIB) patterning and milling was performed using a FEI Strata 400 FIB Ga^+ LIM system. A 2x10 μm Pt strip (~1000 nm thickness) was deposited using the electron gun onto COF films grown on SLG/SiO_2 substrates prior to exposing the sample to the FIB. The sample was then milled with the FIB using a cleaning cross-section. After milling, the samples were imaged at 2 keV using the electron gun. Cross-sectional images were obtained using a stage tilt angle of 52°; thickness measurements made at this angle were corrected by multiplying by 1.26. SLG/SiO_2 substrates were grounded to the sample holder using sticky carbon prior to imaging to minimize charging.

Mass spectra were obtained on a Waters MALDI micro MX MALDI-TOF mass spectrometer using positive ionization and a reflectron detector. MALDI samples were prepared by wet deposition of a saturated analyte/dithranol matrix solution onto a metallic sample plate and air dried before loading into the instrument.

Surface area measurements were conducted on a Micromeritics ASAP 2020 Accelerated Surface Area and Porosimetry Analyzer using ca. 20 mg samples degassed at 180 °C for 12 hours. Nitrogen isotherms were generated by incremental exposure to ultra high purity nitrogen up to ca. 1 atm over 28-hour periods in a liquid nitrogen (77K) bath, and surface parameters were determined using Langmuir, BET and BJH adsorption models included in the instrument software (Micromeritics ASAP 2020 V1.05).

NMR spectra were recorded on a Bruker ARX 300 MHz spectrometer using a standard ^{1}H/X Z-PFG probe at ambient temperature with a 20 Hz sample spin rate.

Solid-state NMR spectra were recorded at ambient temperature on a Varian INOVA-400 spectrometer using an external Kalmus ^{1}H linear pulse amplifier blanked using a spare line. Samples were packed into 7 mm outside diameter silicon nitride rotors and inserted into a Varian HX magic angle spinning (MAS) probe. ^{13}C data was acquired using linearly ramped cross-polarization with MAS (CP/MAS) at 100.5 MHz. The ^{1}H and

^{13}C had ninety-degree pulse widths of 5 μs, and the CP contact time was 1 ms. Two-pulse phase modulation (TPPM) ^{1}H decoupling was applied during data acquisition with a decoupling frequency of 78 kHz. The recycle delays between scans were 2 s. The MAS spin rate varied between 5–7 kHz, as labeled in the spectra. ^{13}C chemical shifts were assigned relative to tetramethylsilane at 0.0 ppm and were calibrated using the methyl carbon signal of hexamethylbenzene assigned at 16.9 ppm as a secondary reference. Direct observation of the ^{11}B nucleus was used to acquire the ^{11}B data at 128.3 MHz. using a pulse width of 1.5 μs, corresponding to a 27° response from the ^{11}B. TPPM decoupling was applied during data acquisition with a decoupling frequency of 78 kHz. A recycle time of 0.6 s was used. The MAS spinning rate varied between 5-7 kHz, as labeled in the spectra. The ^{11}B chemical shifts are assigned relative to $BF_3{\cdot}OEt_2$ at 0.0 ppm and were calibrated using aqueous boric acid at pH = 4.4 assigned at 19.6 ppm as a secondary reference.

Grazing incidence X-ray diffraction (GID) was performed at the G2 station at Cornell High Energy Synchrotron Source (CHESS) using a beam energy of 8.78 ± 0.01 keV (λ = 0.1414 nm), selected using a single-crystal Be crystal monochromator. Motorized slits were used to define a 0.2×2 (V×H) mm^2 beam, with a typical flux of 2×10^{10} photons/s. The data were collected using a 640-element 1D diode-array, of which each element incorporates its own pulse counting electronics capable of count rates of $\sim10^5$ photons/s. A set of 0.1° Soller slits were used on the detector arm to define the in-plane resolution. The scattering geometry is described in detail elsewhere.[1] Each data set was collected by scanning the detector with the sample stationary. The incidence angle α between the beam and sample surface was 0.175°. Axes labels $Q_\perp$ and $Q_\parallel$ are defined using the GISAXS convention $Q_\perp = 4\pi/\lambda\sin(\delta/2)$ and $Q_\parallel = 4\pi/\lambda\sin(\nu/2)$, where δ and ν are the vertical and horizontal scattering angles, respectively.[2] At $\alpha=\delta=0$, $hQ_\parallel$ and $hQ_\perp$ (where h is Planck's constant) are the components of momentum transfer parallel and perpendicular to the sample surface, respectively.

B. Methods and Synthetic Procedures.

Graphene Growth. Single-layer graphene was grown on 25 μm-thick copper foil using previously reported chemical vapor deposition methods.[3] A layer of PMMA (50 nm) was spin-coated on top of the graphene and the copper was etched using aq. $FeCl_3$. The graphene was then transferred to fused SiO_2 and the PMMA removed by washing first with chloroform then isopropyl alcohol. The SLG/SiO_2 was finally calcined at 300 °C for 2.5 h.

General procedure HHTP-DPB film growth on SLG. HHTP **2** (16 mg, 0.049 mmol) and diboronic acid **1** (43 mg, 0.15 mmol) were added to a 15 mL cylindrical pressure vessel and suspended in a mixture of mesitylene and 1,4-dioxane (v/v 1:1; 1.0 mL). After capping, the mixture was sonicated for 30 minutes and a graphene-containing substrate was added. The sealed vessel was heated in a 90 °C oven for 24 h. The vessel was cooled to room temperature and the resulting gray powder was recovered by filtration and dried under vacuum. The graphene-containing substrate was submerged in anhydrous toluene and sonicated for 5 seconds, and finally dried under vacuum.

Scheme S1. Synthesis of boronic acid **1**.

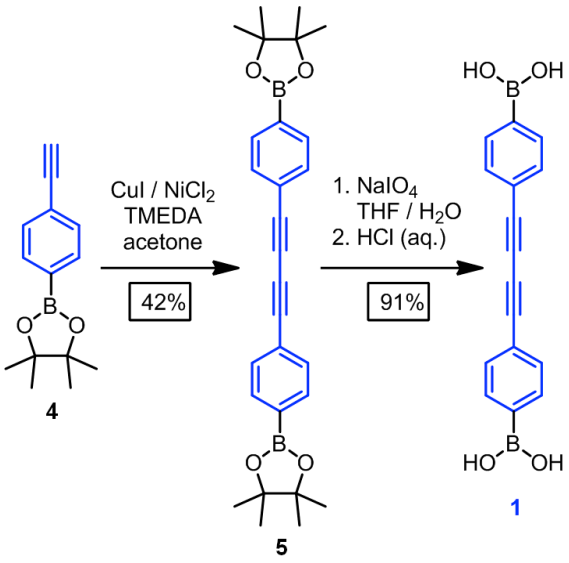

Diboronate ester **5**: TMEDA (0.459 g, 3.946 mmol), CuI (0.188 g, 0.986 mmol), and $NiCl_2$•$6H_2O$ (0.234 g, 0.986 mmol) were dissolved or suspended in $(CH_3)_2CO$ (13 mL) under an atmosphere of air. The mixture became dark green after 10 min. 4-Ethynylbenzeneboronic acid pinacol ester (**4**, 4.50 g, 19.7 mmol) was added, and the mixture was stirred for 12 h. The solvent was evaporated and the resulting yellow-green residue was washed with H_2O (50 mL) and recrystallized from CH_3CN, providing the dialkyne ester **5** (1.90 g, 42%) as a white solid. ^{1}H-NMR ($CDCl_3$, 300 MHz, 298 K) δ 7.65 (d, J = 9.0 Hz, 4H); 7.52 (d, J = 9.0 Hz, 4H); 1.34 (s, 24H). ^{13}C-NMR ($CDCl_3$, 300 MHz) δ 135, 132, 125, 83, 75, 25. MALDI-MS m/z (%) 453.0 (45, M^+); 453.9 (100, M^++1); 454.9 (38, M^++2). IR (powder, ATR) 2981, 2936, 1604, 1542, 1510, 1398, 1355, 1323, 1274, 1261, 1217, 1168, 1141, 1085, 1017, 963, 857, 836, 826, 758, 738 cm^{-1}. UV-Vis [λ /nm (log ε / M^{-1} cm^{-1}), 4.4 μM in DMF] 343 (4.64), 321 (4.75), 300 (4.74), 279(sh) (4.86). Em (λ/nm in DMF) 371, 344. Anal. Calcd for ($C_{28}H_{32}B_2O_4$): C, 74.05; H, 7.10. Found: C, 73.93; H, 6.94.

Diboronic acid **1**: A 20 mL scintillation vial was charged with the diboronate ester **5** (400 mg, 0.88 mmol) and $NaIO_4$ (400 mg, 2.0 mmol). The solids were dissolved in a THF:H_2O mixture (4:1, 6 mL) and stirred at rt for 2 h. 1M HCl (2 mL) was then added via micropipette to the white suspension, which was stirred for another 12 h. The pale

yellow-white suspension was diluted with H_2O (20 mL), and the solids recovered by filtration. The recovered solid was washed with an additional H_2O (20 mL) followed by hexanes (10 mL). The white solid was dried under vacuum to yield 233 mg (91%) of boronic acid **1**. ^{1}H-NMR (DMSO-d_6, 300 MHz) δ 8.26 (s, 4H); 7.82 (d, J = 7.5 Hz, 4H); 7.57 (d, J = 7.5 Hz, 4H). ^{13}C-NMR (DMSO-d_6, 300 MHz) δ 136, 134, 131, 122, 82, 74. MALDI-MS m/z (%) 289.1 (21, M^+); 290.1 (100, M^++1); 291.1 (2, M^++2). IR (powder, ATR) 3391, 3315, 1604, 1545, 1509, 1399, 1337, 1263, 1215, 1162, 1121, 1084, 1027, 1012, 972, 859, 834, 809, 757, 738 cm^{-1}. UV-Vis [λ /nm (log ε / M^{-1} cm^{-1}), 7.6 μM in DMF] 341 (4.77), 319 (4.85), 299 (4.76), 277(sh) (4.77). Em (λ/nm in DMF, λ_{ex} = 350 nm) 372, 390, 402. Anal. Calcd for ($C_{16}H_{12}B_2O_4$): C, 66.29; H, 4.17. Found: C, 66.08; H, 4.03.

HHTP-DPB COF: Boronic acid **1** (20 mg, 0.069 mmol) and HHTP **2** (7 mg, 0.022 mmol) were combined in a mixture of dioxane and mesitylene (1:1, 4 mL) and sonicated for 10 min. The light gray suspension was transferred to a 10 mL pre-scored long-necked glass ampoule, flash-frozen in a liquid nitrogen bath, and flame-sealed. The ampoule was placed in a 90 °C gravity convection oven for 72 h, and the resulting free-flowing tan powder was collected by filtration on a Hirsch funnel, washed with 1 mL anhydrous toluene and air-dried. The crude **HHTP-DPB COF** was characterized by PXRD and IR before and after heating at 100 °C under vacuum. Isolated yield 10 mg (71%). IR (powder, ATR) 1606, 1493, 1452, 1355, 1326, 1243, 1161, 1065, 1018, 832, 734 cm^{-1}. PXRD [2θ (relative intensity)] 2.17 (100), 3.29 (26), 5.90 (8.0), 8.02 (2.7), 9.68 (1.60), 11.66 (0.86), 25.84 (0.74). UV-Vis (powder, praying mantis DRA) 1069, 989, 615 (sh), 369. Em (λ/nm, λ_{ex} = 350 nm) 463. Anal. Calcd for $(C_{42}H_{18}B_3O_6)_n$: C, 77.49; H, 2.79. Found: C, 72.57; H, 3.04. It has been noted[4,5] that elemental analysis of boronate COFs typically give lowered carbon values from the formation of non-combustible boron carbide byproducts. The presence of boron was confirmed by a characteristic B 1s peak in the XPS with a binding energy of 190.6 eV.

C. NMR Spectra.

Figure S1. ^{1}H-NMR spectrum of ester **5** ($CDCl_3$, 500 MHz, 298K).

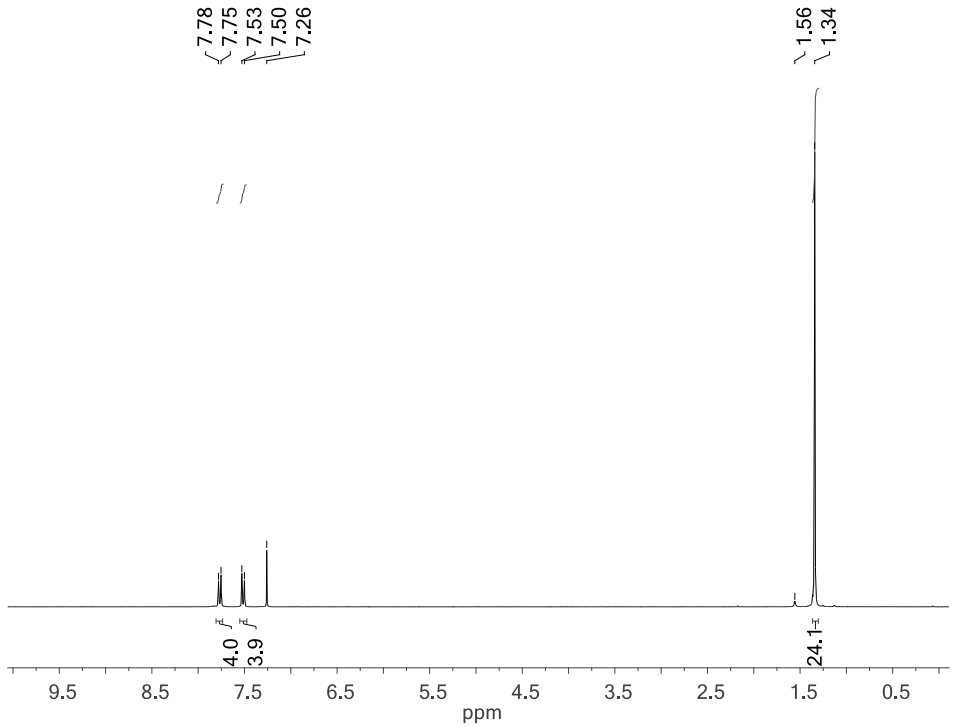

Figure S2. ^{13}C-NMR spectrum of ester **5** ($CDCl_3$, 500 MHz, 298K).

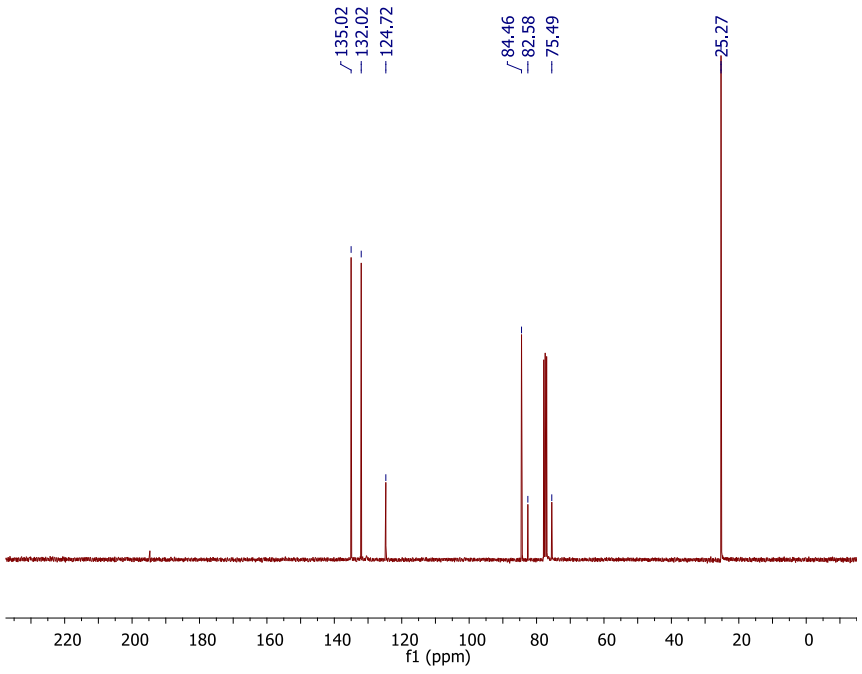

Figure S3. [1]H-NMR spectrum of acid **1** (DMSO-d_6, 500 MHz, 298K).

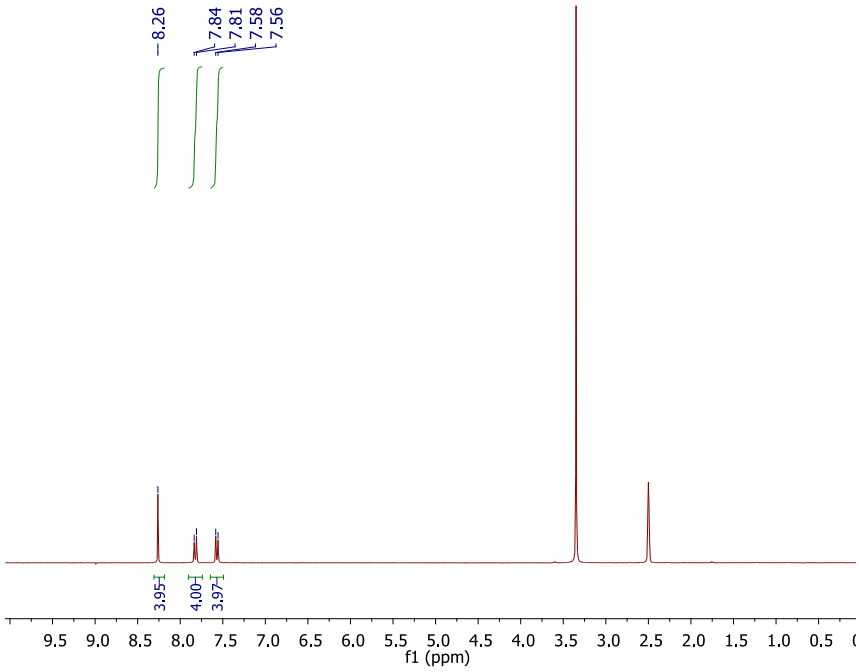

Figure S4. [13]C-NMR spectrum of acid **1** (DMSO-d_6, 500 MHz, 298K).

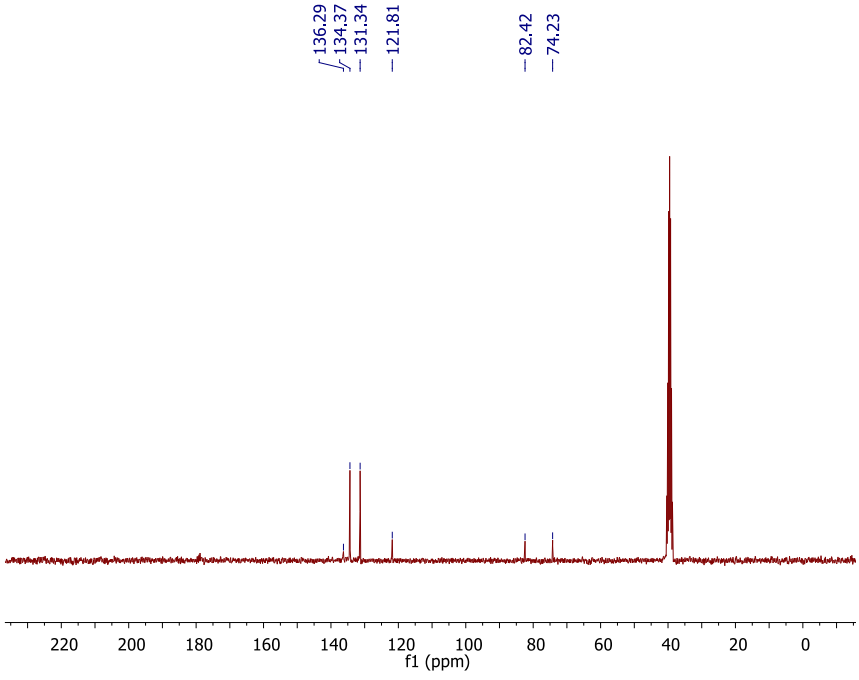

D. MALDI-TOF MS of COF Precursors

Figure S5. MALDI-MS spectrum of ester **5**.

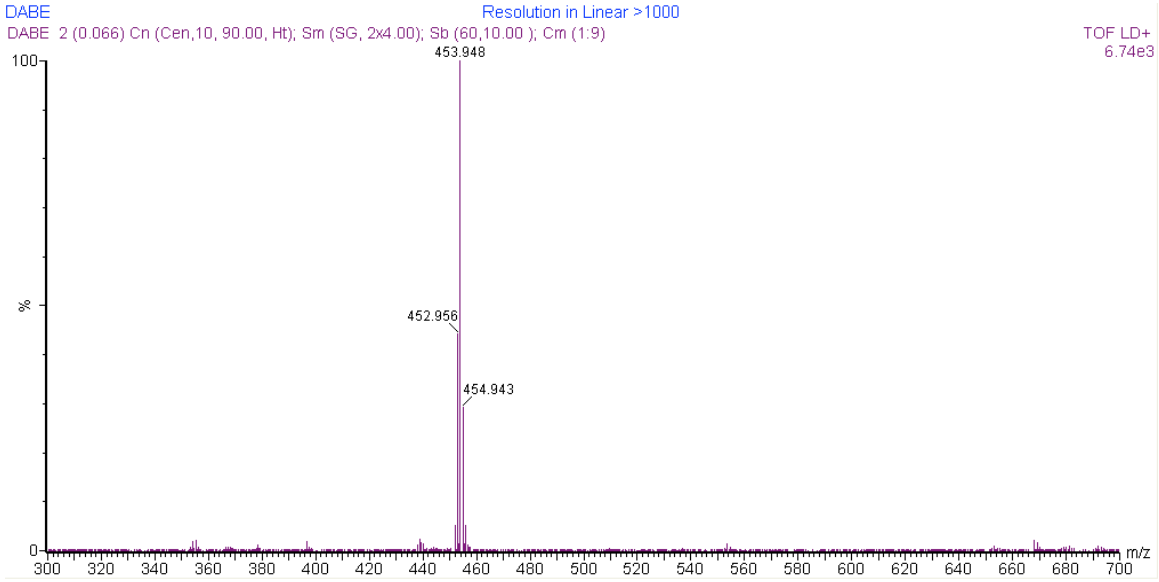

Figure S6. MALDI-MS spectrum of acid **1**.

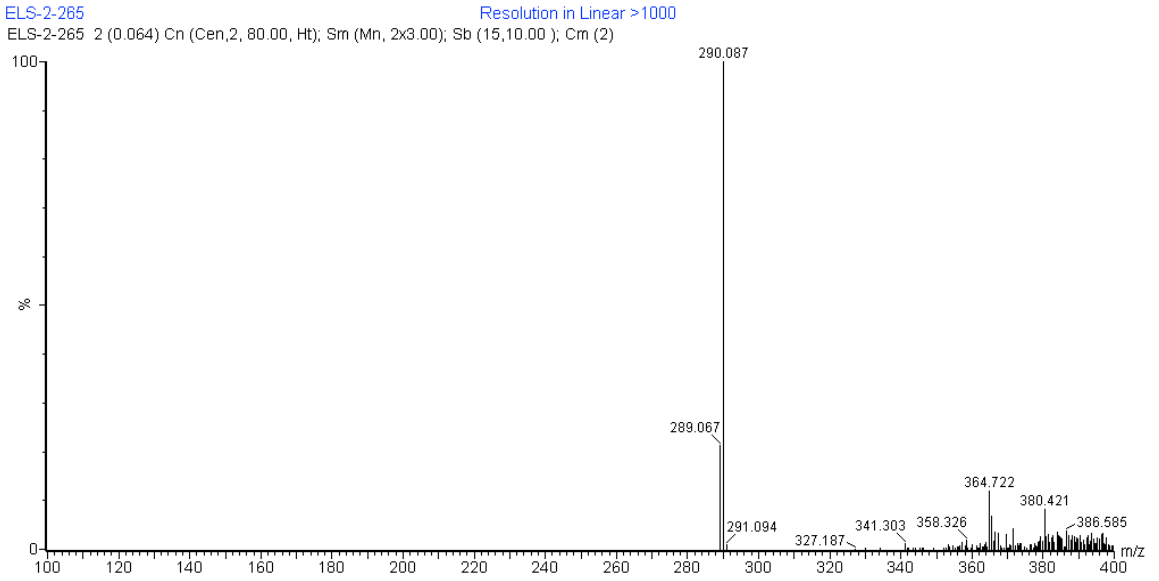

E. Solid-state CP/MAS ^{13}C and ^{11}B NMR of HHTP-DPB COF

Figure S7. CP/MAS ^{13}C NMR spectra of **HHTP-DPB COF** prior to activation (note presence of mesitylene). The spectra were acquired at two different spinning rates to assign spinning side bands (*).

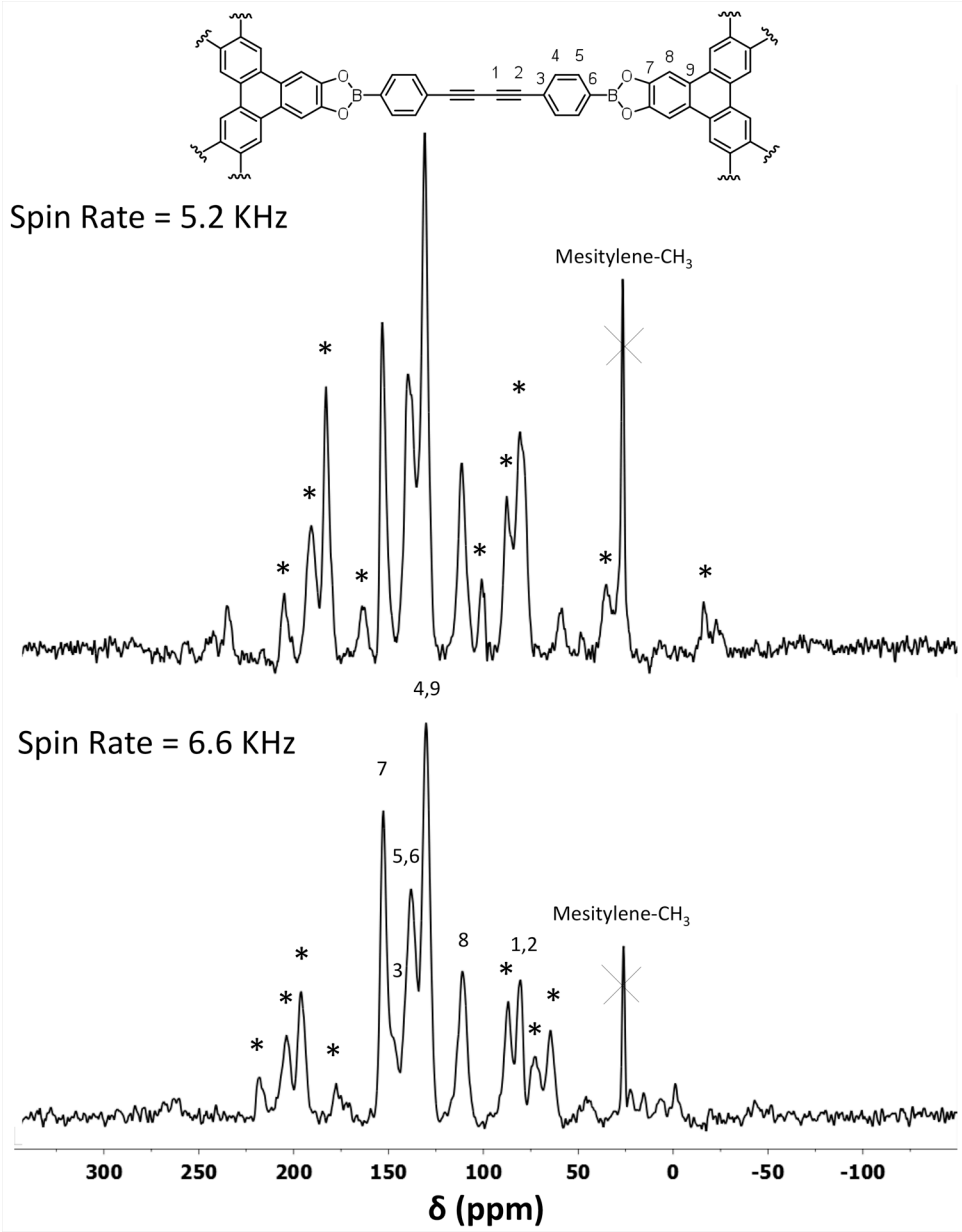

Figure S8. CP/MAS ^{13}C NMR spectra of **HHTP-DPB COF** after activation. The spectra were acquired at two different spinning rates to assign spinning side bands (*).

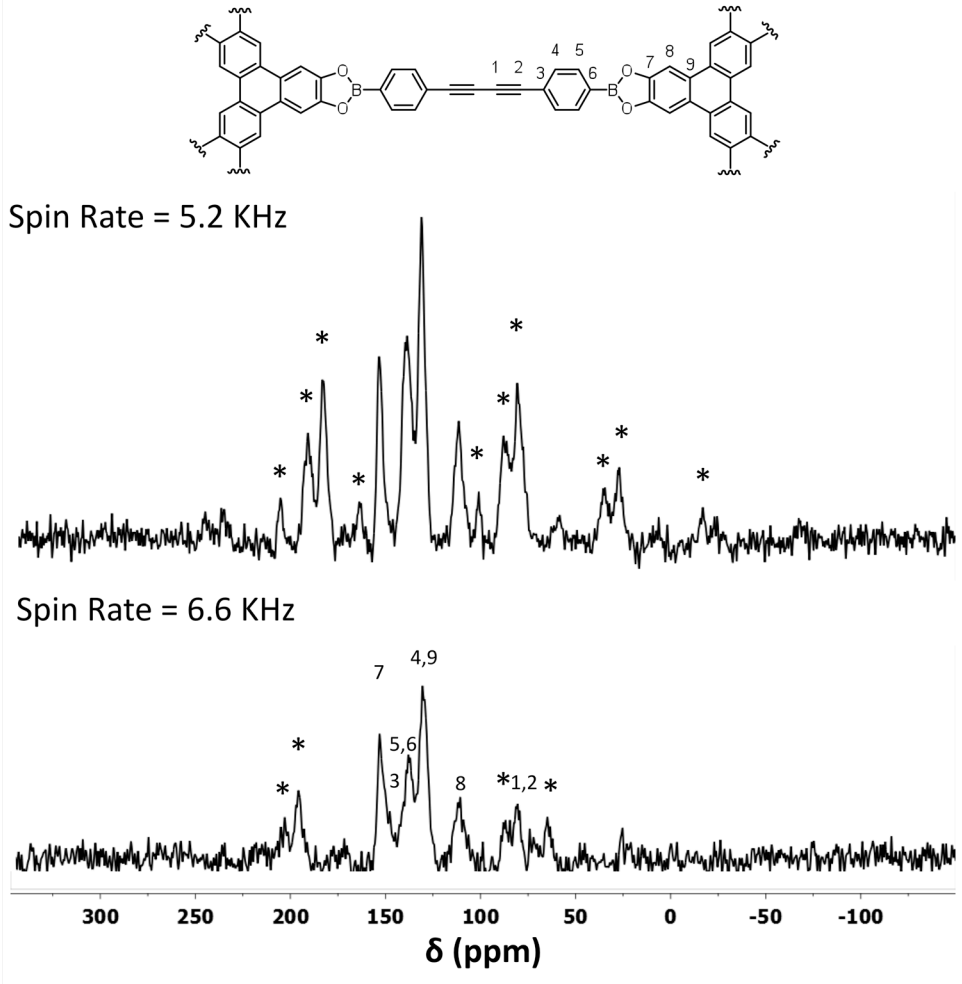

Figure S9. Solid-state ^{11}B NMR spectra of **HHTP-DPB COF** prior to activation. The spectra were acquired at two different spinning rates to assign spinning side bands (*).

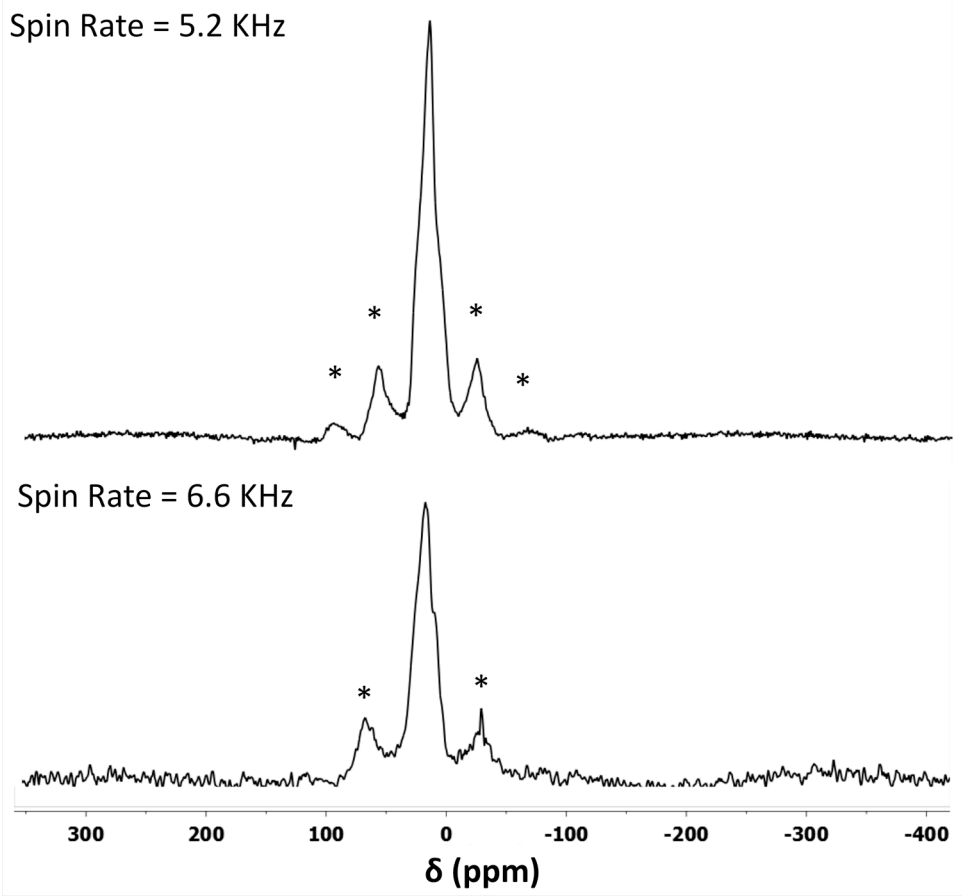

F. FTIR Spectra.

Figure S10. FTIR spectra of diboronate ester **5** (blue) and acid **1** (red).

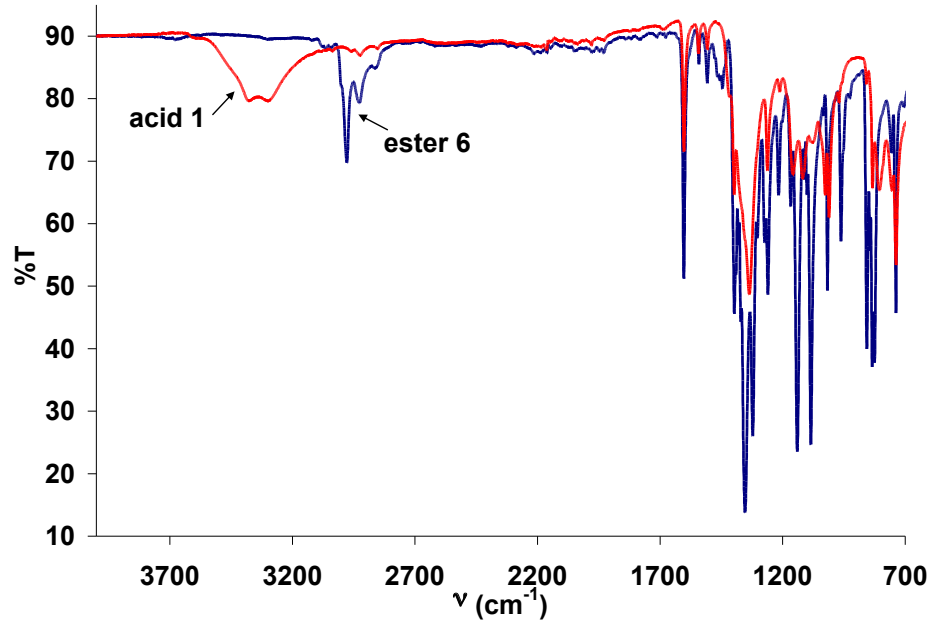

Figure S11. FTIR spectra of **HHTP-DPB COF** before (blue) and after (red) pore activation by heating under vacuum.

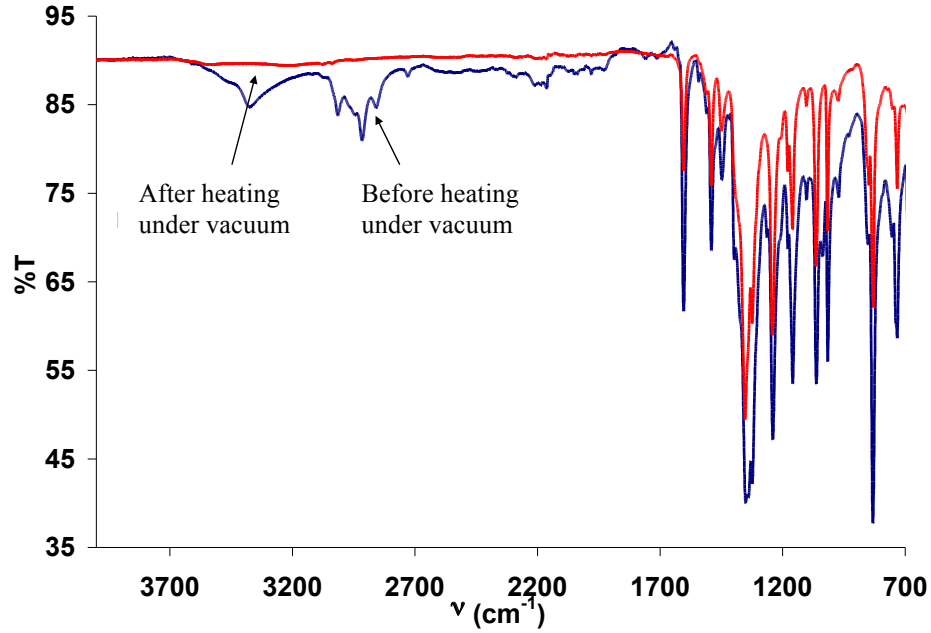

G. UV-Vis-NIR Characterization

Figure S12. Absorption spectra of ester **5** (blue) and acid **1** (red) in DMF.

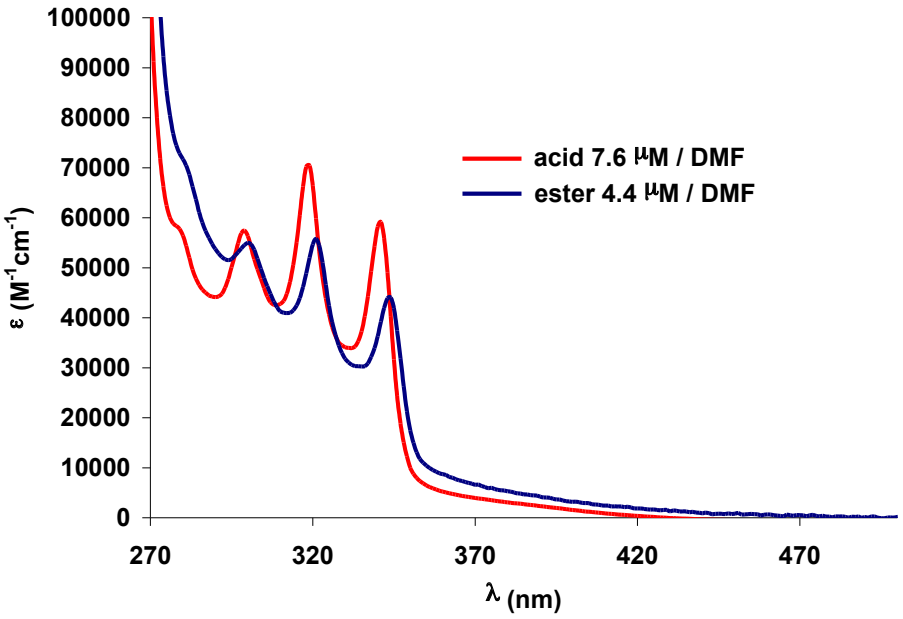

Figure S13. Absorption spectrum of HHTP **2** in DMF.

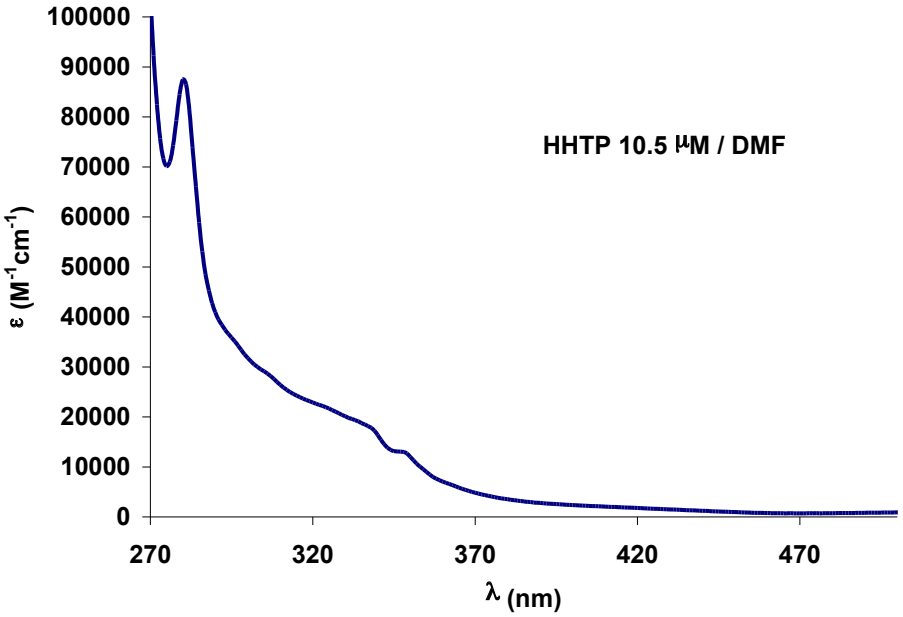

H. Emission Spectra.

Figure S14. Emission spectra (λ_{exc} = 350 nm) of acid **1** (blue), ester **5** (green), and HHTP **2** (gold) in DMF.

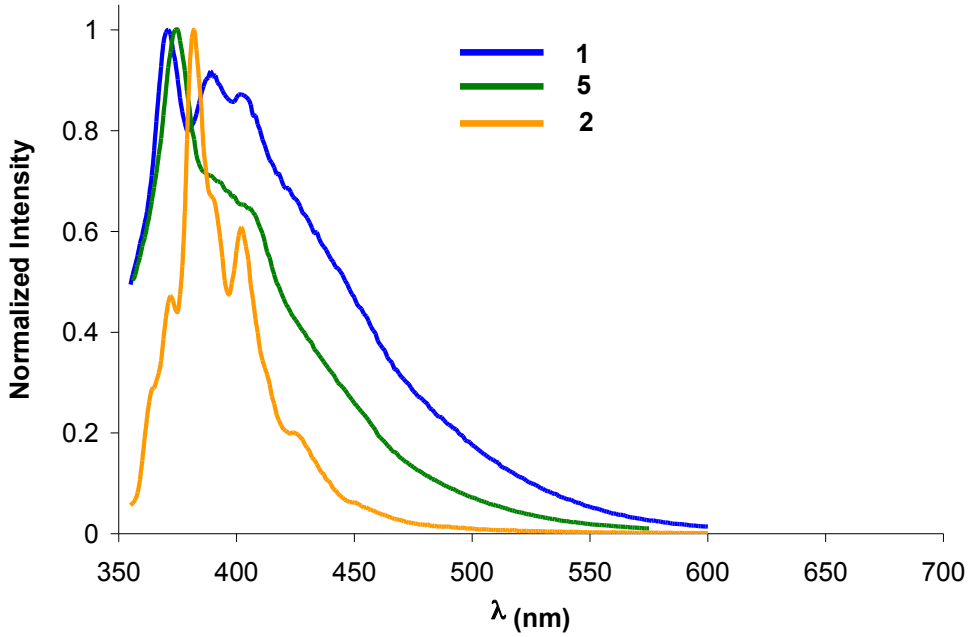

I. Powder X-Ray Diffraction Data.

Figure S15. PXRD pattern of initially isolated **HHTP-DPB COF** material before pore activation (blue) vs simulated pattern (red). Note significant amount of amorphous material and impurities.

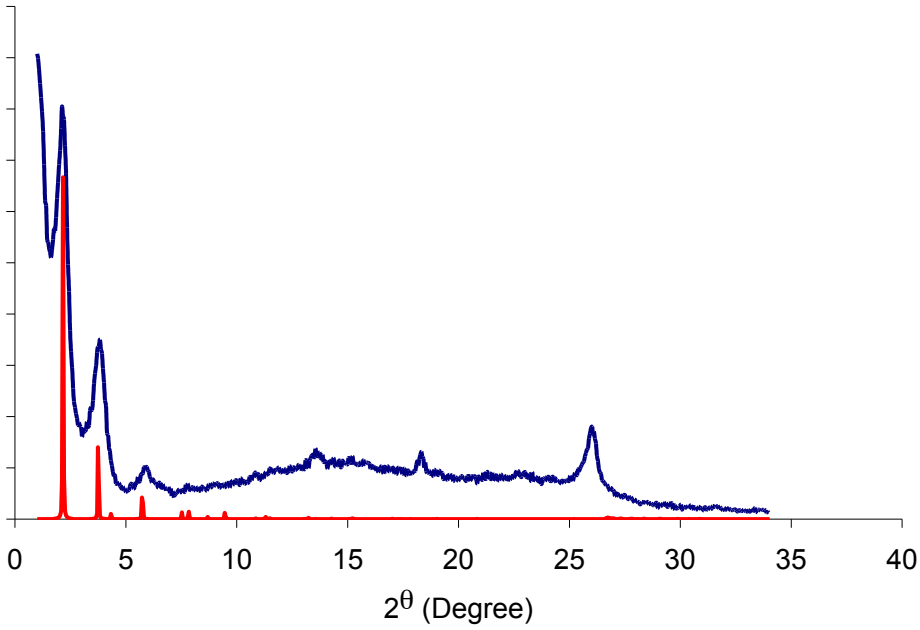

J. Simulation of the COF Structures from X-ray Diffraction Data. Molecular modeling of the COF was carried out using the Materials Studio (ver.5.0) suite of programs by Accelrys.[6] The unit cell precursor was defined as the model structures shown in Figure S22a. The initial structures (**bnn**) were constructed piecewise starting with a primitive hexagonal unit cell with space group *P*6/*mmm*. The *a* cell parameter was estimated according to the distance between the center of the vertices for each COF as shown in Figure S13, and *c* parameter was arbitrarily chosen as 3.35 Å. The structures were optimized using the Geometry Optimization routine including energy minimization with cell parameters optimization, using the parameters from the Universal Force Field.[8] Modeling of the staggered structures (**gra**) was performed in a similar manner but starting with the space group $P6_3/mmc$, and $c = 6.70$ Å. The MS Reflex Plus module was then used to calculate the expected PXRD patterns, which matched the experimentally observed pattern closely in peak position and intensity (line broadening from crystallite size was not calculated). The observed diffraction pattern was subjected to Pawley refinement wherein peak profile and line shape parameters were refined using the Pseudo-Voigt peak shape function and asymmetry was corrected using the Berar-Baldinozzi function.[4,7] The refinement was applied to the calculated lattice, producing the refined PXRD profile.

Figure S16. Precursor structure used for initial modeling of the COF structure.

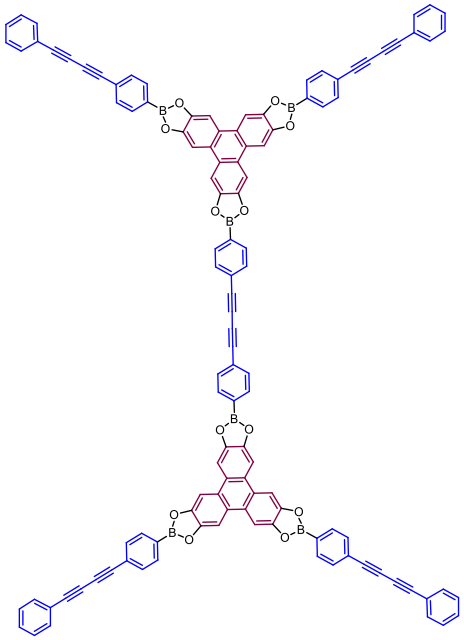

Figure S17. COF crystal model in **bnn** configuration.

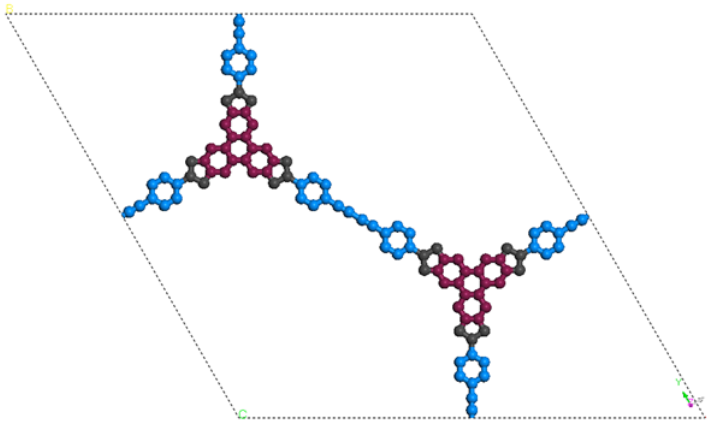

HHTP-DPB COF

Figure S18. Observed (blue) versus Pawley-refined (red) PXRD pattern profiles for **HHTP-DPB COF**.

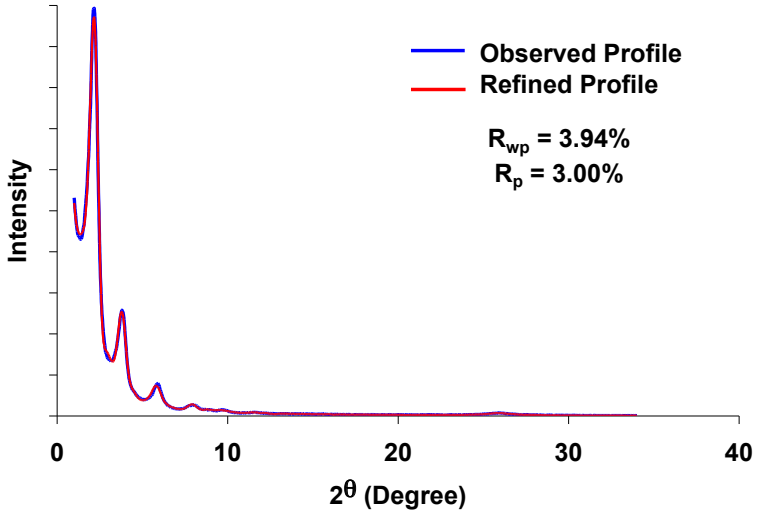

Table S1. Fractional atomic coordinates for unit cell of **HHTP-DPB COF** calculated using the Materials Studio ver. 5.0 modeling program.

bnn
(*P*6/*mmm*)
a = *b* = 46.909 Å, *c* = 3.369 Å

atom	*x*	*y*	*z*
C1	0.980992	0.490590	0.50000
C2	0.950829	0.475552	0.50000
C3	0.914652	0.457440	0.50000
C4	0.896801	0.474121	0.50000
C5	0.862091	0.456695	0.50000
C6	0.844338	0.422146	0.50000
C7	0.755507	0.391306	0.50000
C8	0.726037	0.392127	0.50000
C9	0.695359	0.362223	0.50000
B1	0.804937	0.402202	0.50000
O1	0.785010	0.366023	0.50000

Figure S19. Model (top) of **HHTP-DPB COF** in a **gra** packing and corresponding simulated PXRD pattern (bottom).

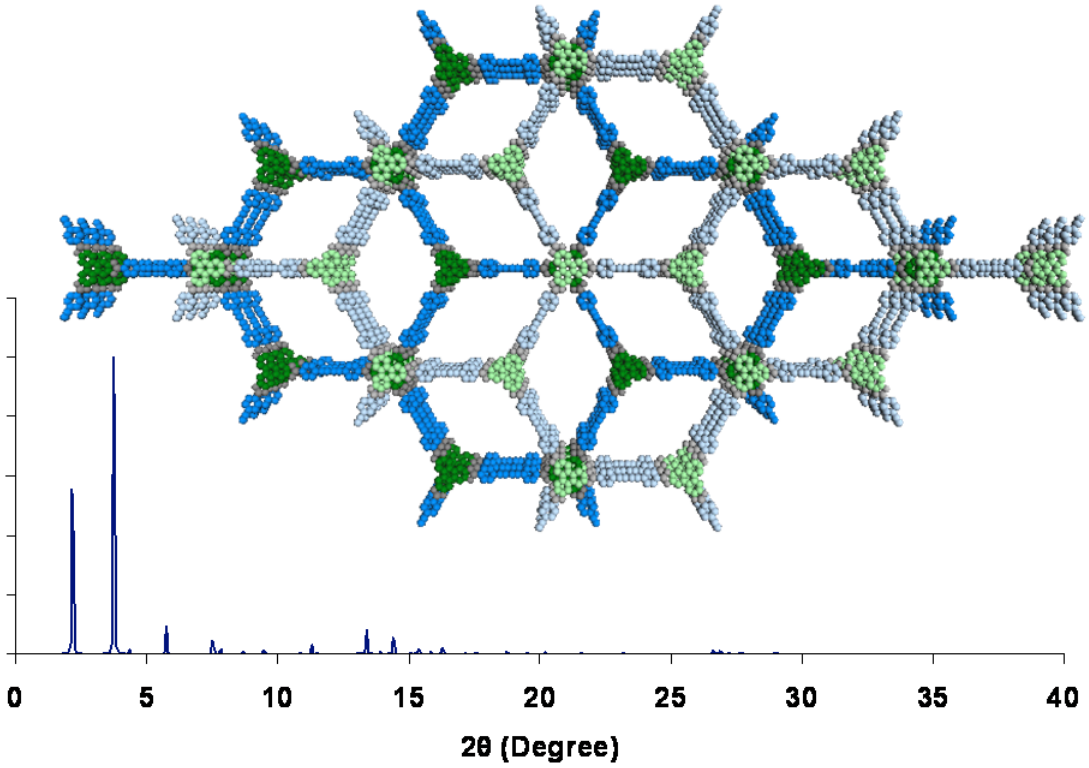

K. Thermogravimetric Analysis. TGA trace of the COF was obtained up to 700 °C using a linear 10 °C/min ramp method.

Figure S20. Thermogravimetric trace of **HHTP-DPB COF**.

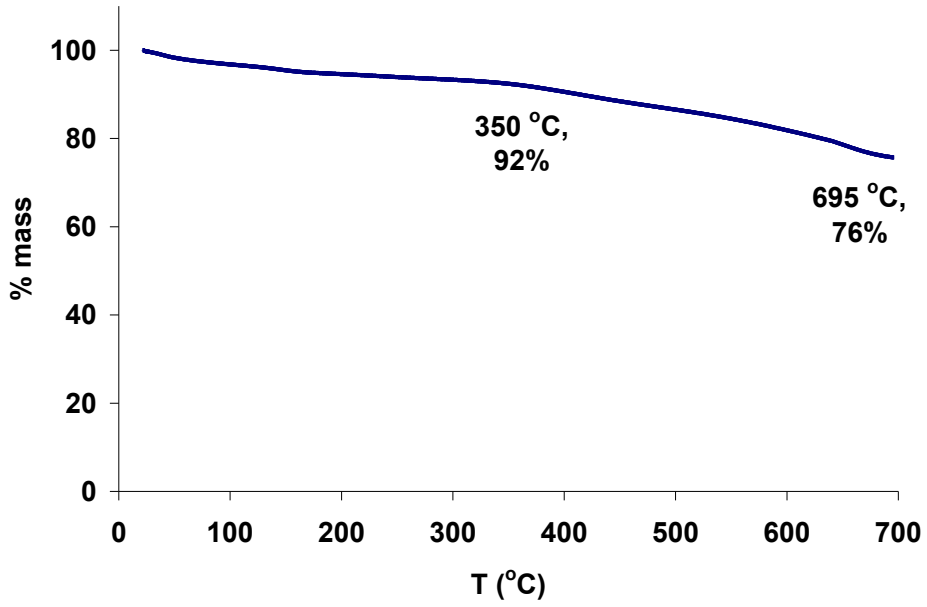

L. Surface Area Measurements and Simulations.

Figure S21. Langmuir and BET surface area plot for **HHTP-DPB COF** calculated from adsorption data.

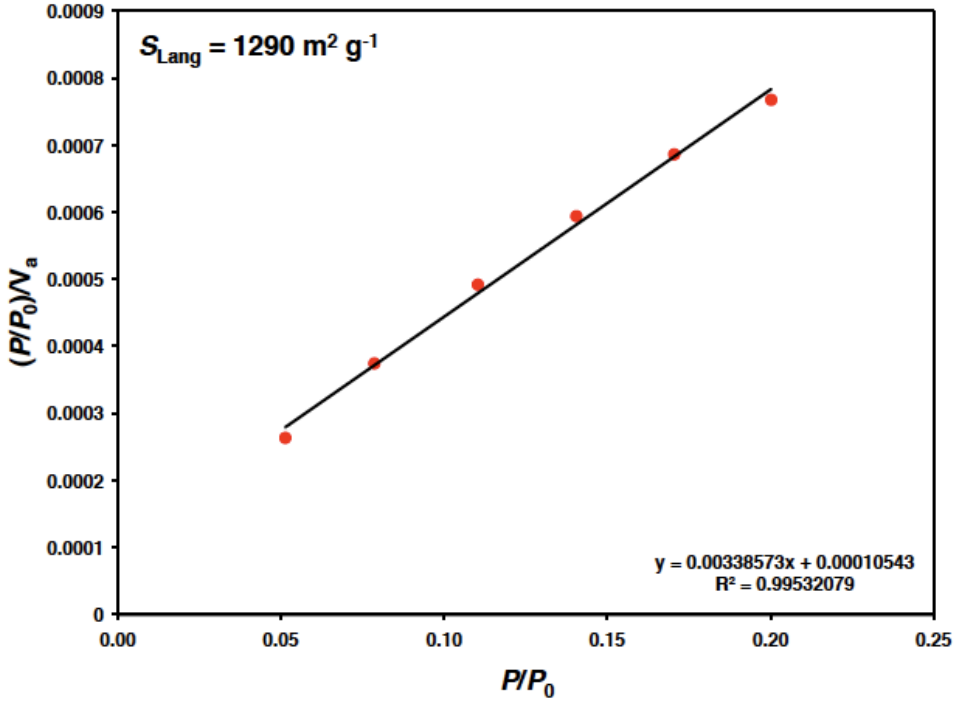

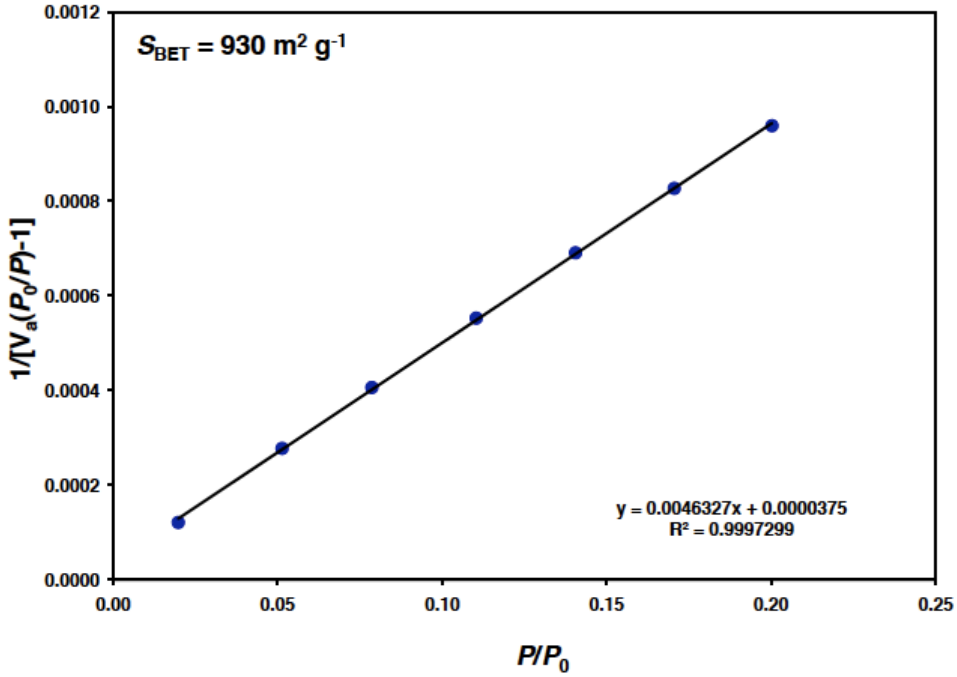

Simulations of the N_2 Isotherm of HHTP-DPB COF

Simulations of the N_2 adsorption isotherm was performed using Monte Carlo Metropolis method[9] using the Sorption Module in Materials Studio. 100 adsorption steps in logarithmic scale were simulated using 10^5 equilibration steps and 10^6 production steps at 77 K for N_2. The relaxed structures obtained from crystal modeling and dinitrogen adsorbate were used as inputs for the simulation using the parameters in the universal force field (UFF).[8] For the final isotherms, the fugacity was transformed into P/P_0 units and loading per cell was transformed into cm^3 (STP) g^{-1} units. The Brunauer-Emmett-Teller (BET) model was used over the obtained isotherms in the $0.05 < P/P_0 < 0.30$ ranges to obtain the BET surface area.

The accessible surface area was calculated in Materials Studio by determining the Connolly surface of the crystal models using a probe with a radius of 1.6 Å. In addition to the fully eclipsed *P*6/*mmm* (**bnn**) structure, accessible surfaces of crystal models were calculated of the fully staggered structure $P6_3/mmc$ (**gra**) and the eclipsed structure after reducing the symmetry of a super cell ($a' = a$, and $c' = 2c$) to *P*1 and inducing offsets between the two independent layers present.

Figure S22. Simulated N_2 adsorption isotherm of **HHTP-DPB-COF**.

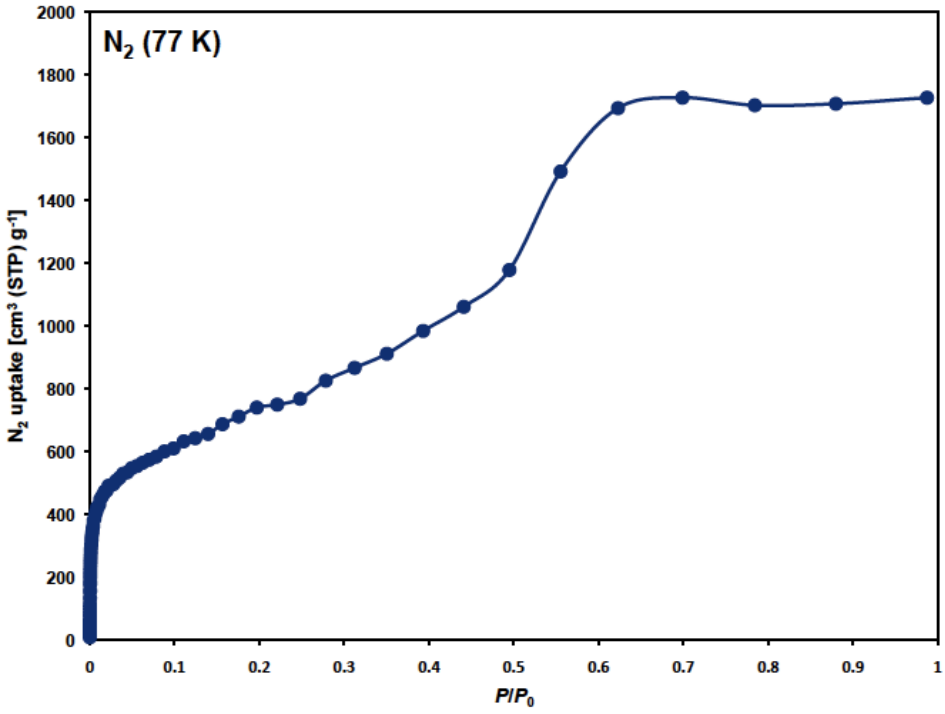

Figure S23. BET plot of the simulated N_2 adsorption isotherm of **HHTP-DPB-COF**. Surface area and linear equation inset.

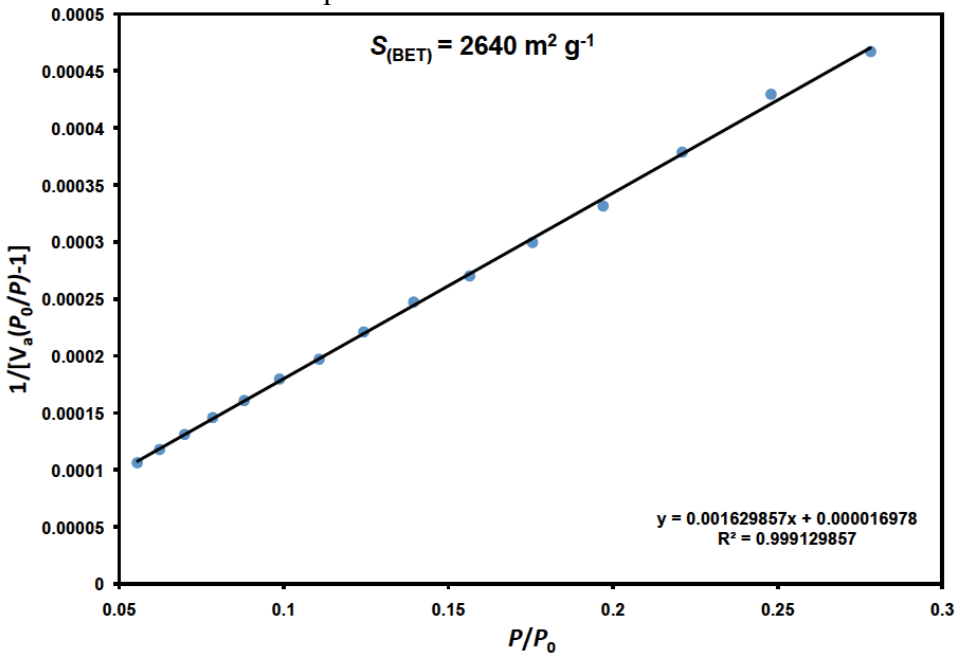

Table S2. Accessible surface areas obtained from the Connolly surfaces of the crystal models.

Structure	Accessible Surface Area (m^2 g^{-1})
*P*6/*mmm* (**bnn**)	2669.5
$P6_3/mmc$ (**gra**)	9206.7
*P*1 (eclipsed w/offset by 1Å *a* + 1 Å *b*)	2689.4
*P*1 (eclipsed w/offset by 1.7 Å to center of pore)	2709.6

M. Computational Methods

We computed the potential energy surface (PES) describing the offset of **HHTP-DPB COF** layers with two independent approaches: density functional theory (DFT) and molecular mechanics (MM). Preceding the PES calculations, the geometry of a single HHTP-DPB layer was optimized in Gaussian09[12] with DFT using the M06[13] exchange correlation functional and the 6-31G(d,p) basis set. M06 is a meta-hybrid generalized gradient approximation functional that has been designed to accurately model non-covalent interactions and has been used in prior studies to model molecular systems with π-π stacking.[12] Therefore, in addition to the modeling of intramolecular interactions, the M06 functional was used to model the intermolecular interactions between layers, given the highly aromatic structure of **HHTP-DPB COF**. To generate the PES with molecular mechanics methods, we implemented the intermolecular portion of the semi-empirical Molecular Mechanics 3 (MM3) force field[13] in the LAMMPS software package.[14] The MM3 force field was chosen based on our prior experience applying it to hydrocarbon and aromatic systems, where results were comparable to *ab initio* MP2-derived intermolecular energies.[15] The two intermolecular interactions described in MM3 are van der Waals and bond dipole interactions, which are implemented as a Buckingham potential and a dipole-dipole term from the series expansion of the electrostatic potential, respectively. We modified the force field by replacing the bond dipole interaction terms with relatively stronger atomic monopole interactions derived from CHelpG[16] partial charges to more accurately model the electrostatic interactions. The CHelpG partial charges were computed at the level of B3LYP/6-31G(d,p). The MM3 force field provides a complete, though phenomenological, description of the intermolecular interactions for all common covalent organic framework atoms, such as boron, carbon, hydrogen, and oxygen.

To determine the structure of the **HHTP-DPB COF** layer using DFT, we combined the individually optimized geometries of a diphenylbutadiyne linker and a HHTP/phenylene COF (COF-5) as shown in Fig. S19A by replacing the phenylene "linker" in COF-5 with the longer diphenylbutadiyne linker and increasing the size of the unit cell accordingly. The geometry of the composite **HHTP-DPB COF** structure is shown in Fig. S19B. The C-C bond lengths of the two aromatic rings of the

diphenylbutadiyne linker differ from the C-C bond lengths of the phenylene linker by no more than 0.01 Å, so we are confident that the composite **HHTP-DPB COF** structure is an accurate representation of the structure obtained by a geometry optimization of the full **HHTP-DPB COF**. Also, the composite **HHTP-DPB COF** structure produces a pore size of 46 Å, which is similar to the experimentally obtained pore size.

The two-layer configurations on which the semi-empirical MM calculations were performed consisted of 276 atoms, with 138 atoms per layer adopting the geometry obtained from DFT. Each layer was represented with a monoclinic unit cell with a lattice parameter of 46.3 Å along the *a* and *b* crystallographic axes and a γ of 60°. The system was slab-like with vacuum above and below to limit the intermolecular interactions to first and second layer interactions. In each intermolecular potential energy calculation, the layers were assumed to retain their exact geometry, so further geometry relaxations were not performed.

To generate the PES, atoms in the bottom layer of the stacked system were held rigidly in place while the top layer was translated over the surface of the other in increments of 0.1 Å along both *a* and *b* axes. At each *a* and *b* offset, the layer spacing (*c*-axis) was shifted from 2.50 Å to 4.00 Å in increments of 0.01 Å, and the intermolecular potential energies were computed. The lowest energy configurations along the *c*-axis were projected onto the *ab* plane to be able to visualize the 3-dimensional data in two dimensions. The range of layer spacing probed was wide enough to include all minimum energy structures. The layer spacing was continuous across the PES and ranged from 3.2 to 3.5 Å. Layer rotations were not considered while constructing the PES because the resulting loss of order would be computationally intractable to model. After analysis of the PES corresponding to only translational offsets, we concluded that the disruption in symmetry from layer rotations would also result in less overlap between the layers leading to a smaller and more unfavorable van der Waals interaction. As a further assumption, we hypothesized that the intermolecular interactions between non-adjacent layers would not contribute significantly to the PES since a doubling of the layer spacing reduces the intermolecular energy to less than 10% of its original value, which allows us to use just two layers in the simulation of layer-layer stacking.

Eclipsed (**bnn**) and staggered (**gra**) structures were explored in greater detail with DFT by calculating the potential energy of representative fragments of a two-layer system. We fashioned dimers out of small fragments taken from the full COF layer, consisting of one HHTP unit and either three half-sized hydrogen-capped linkers (for eclipsed calculations) or three full-sized hydrogen-capped linkers (for staggered calculations), as shown in Fig. S19C and S19D, respectively. We used layer fragments instead of complete layers to probe the PES since it constrained the number of atoms to a more computationally tractable size; given the symmetry in the COF structure, and the rigidity of the overall COF, we believe that this approach of considering only part of the COF is an acceptable compromise. For calculations of eclipsed dimers, the potential energy was doubled to match the energy obtained from the larger system size in the molecular mechanics simulations. For calculations of staggered dimers, the potential energy of dimers was not doubled, since the number of HHTP-HHTP interactions matched that of the molecular mechanics simulations. The same procedure followed for the MM3 model was used to generate the PES from the **HHTP-DPB COF** layer fragments. Dimers with translational offsets within a 3 Å radius of the center of the PES were tested with a resolution of 0.1×0.1 $Å^2$, and the dimer spacing was shifted in increments of 0.01 Å, after which the lowest energy configurations were projected onto the x-y plane. The PES for the staggered layer configurations was generated by testing translational offsets within a 3 Å radius of a perfectly staggered structure.

Figure S24.

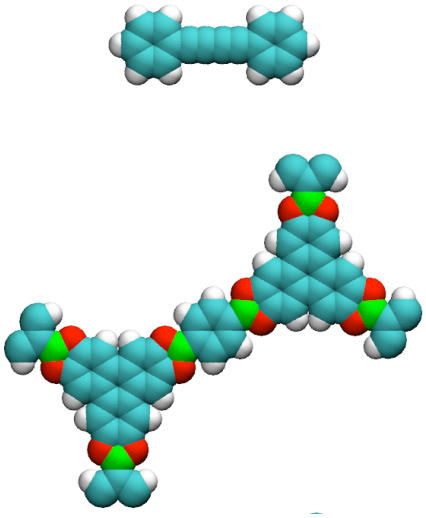

A. Structure of a hydrogen-capped diphenylbutadiyne linker and an HHTP-phenylene (COF-5) covalent organic framework used to build the unit cell structure of the **HHTP-DPB COF**.

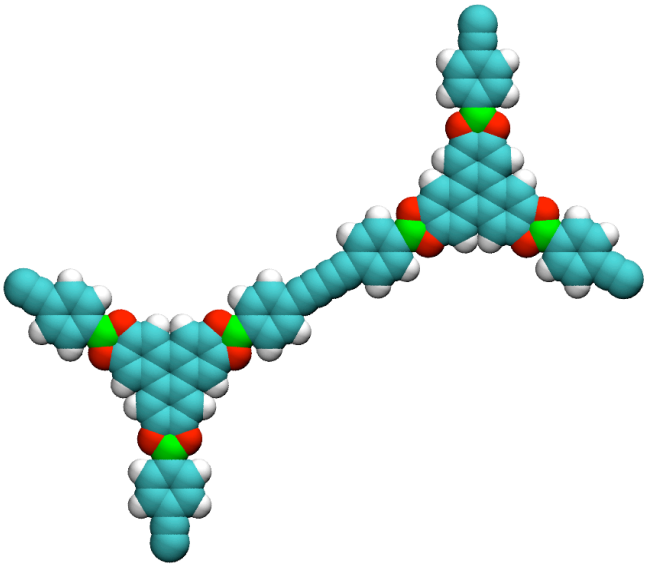

B. Structure of one unit cell of the **HHTP-DPB COF** used in the molecular mechanics simulations.

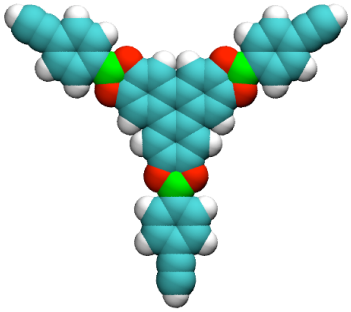

C. Structure of one layer fragment of the **HHTP-DPB COF** with half-sized hydrogen capped linkers used in the ab initio simulation of eclipsed layers.

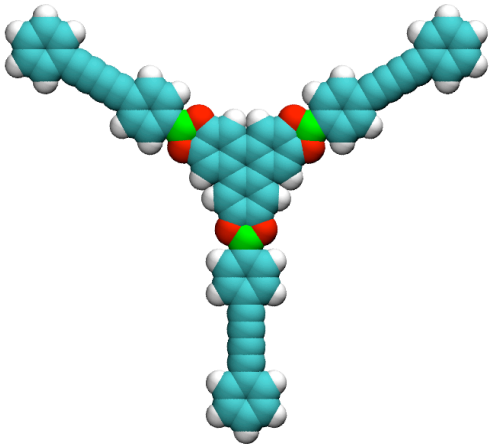

D. Structure of one layer fragment of the **HHTP-DPB COF** with full-sized hydrogen capped linkers used in the ab initio simulation of staggered layers.

N. Film Characterization

Figure S25. GID of **HHTP-DPB COF** thin film (growth time: 24 h).

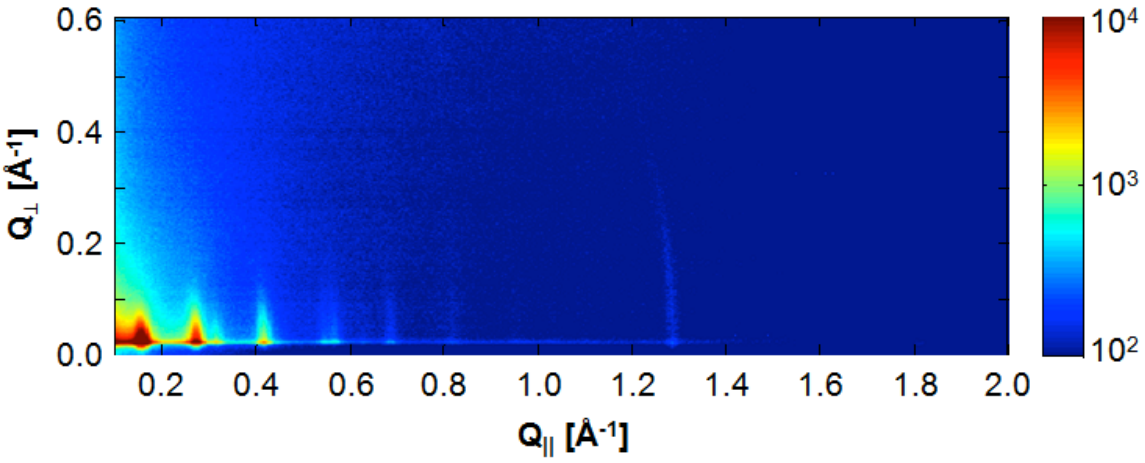

Figure S26. GID data obtained at large $Q_\perp$, showing the off-specular projection of the **HHTP-DPB COF** film (001) Bragg peak (growth time: 24 h).

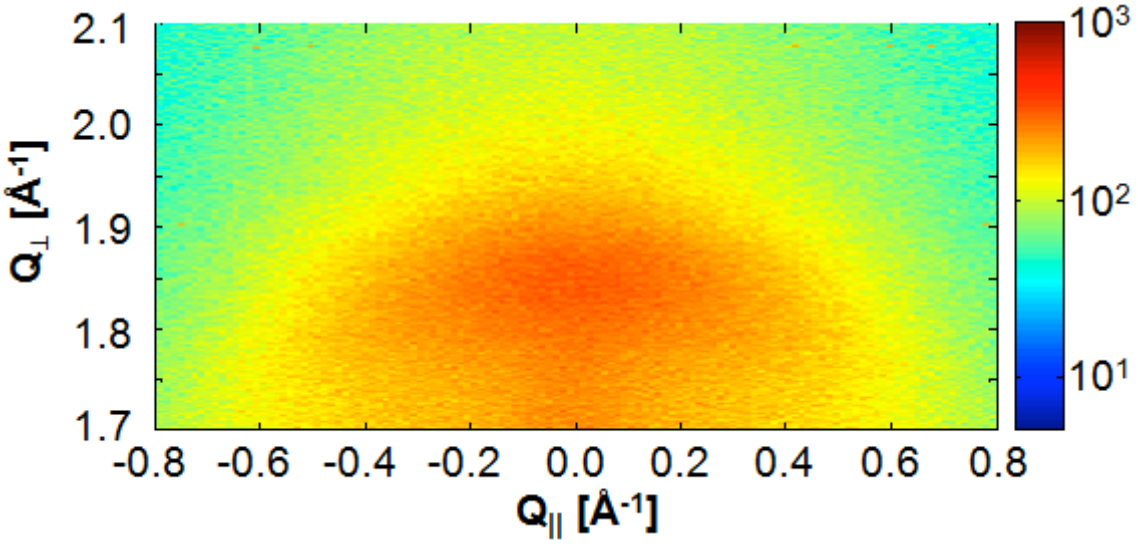

Figure S27. Top down SEM of **HHTP-DPB COF** thin film on SLG (growth time: 24 h).

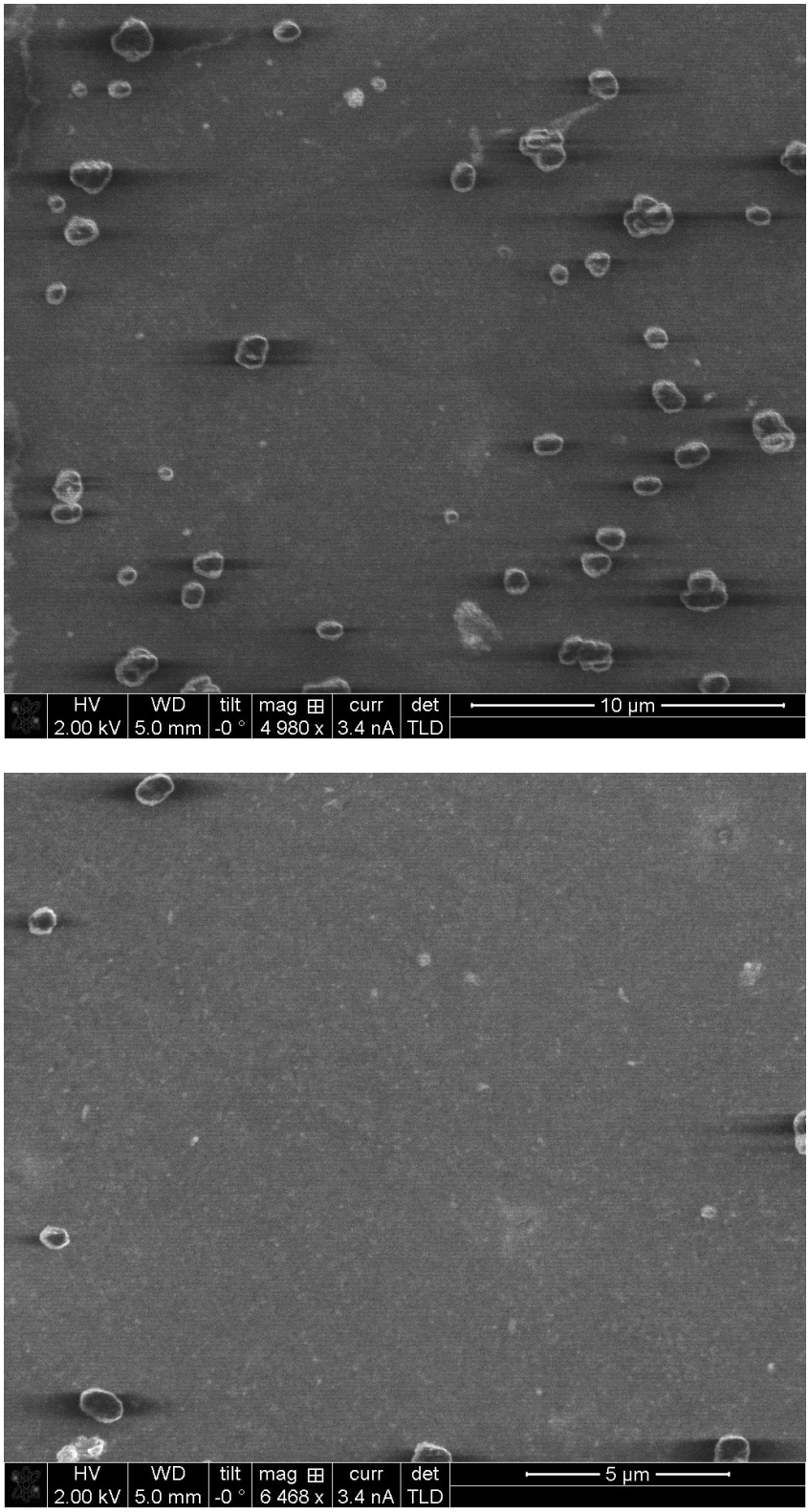

O. References.

[1] D. M. Smilgies, D. R. Blasini, S. Hotta, H. Yanagi, *J. Synchrotron Rad.* **2005**, *12*, 807.

[2] D. M. Smilgies, D. R. Blasini, *J. Appl. Crystallogr.* **2007**, *40*, 716.

[3] a) X. S. Li, W. W. Cai, J. H. An, S. Kim, J. Nah, D. X. Yang, R. Piner, A. Velamakanni, I. Jung, E. Tutuc, S. K. Banerjee, L. Colombo, R. S. Ruoff, *Science* **2009**, *324*, 1312; b) M. P. Levendorf, C. S. Ruiz-Vargas, S. Garg, J. Park, *Nano Lett.* **2009**, *9*, 4479.

[4] E. L. Spitler, W. R. Dichtel, *Nat. Chem.* **2010**, *2*, 672.

[5] A. P. Côté, A. I. Benin, N. W. Ockwig, M. O'Keeffe, A. J. Matzger, O. M. Yaghi, *Science* **2005**, *310*, 1166.

[6] Accelrys, 4.4 ed., Accelrys Software, San Diego, **2008**.

[7] S. Wan, J. Guo, J. Kim, H. Ihee, D. L. Jiang, *Angew. Chem. Int. Ed.* **2008**, *47*.

[8] Metropolis, N., Rosenbluth, A. W., Rosenbluth, M. N., Telle, A. H., Teller, E. *J. Chem. Phys.* **1953**, *21*, 1087.

[9] Rappe, A. K., Casewit, C. J., Colwell, K. S., Goddard-III, W. A., Skiff, W. M. *J. Am. Chem. Soc*. **1992,** *114,* 10024.

[10] Gaussian 09, Revision A.02, M. J. Frisch, G. W. Trucks, H. B. Schlegel, G. E. Scuseria, M. A. Robb, J. R. Cheeseman, G. Scalmani, V. Barone, B. Mennucci, G. A. Petersson, H. Nakatsuji, M. Caricato, X. Li, H. P. Hratchian, A. F. Izmaylov, J. Bloino, G. Zheng, J. L. Sonnenberg, M. Hada, M. Ehara, K. Toyota, R. Fukuda, J. Hasegawa, M. Ishida, T. Nakajima, Y. Honda, O. Kitao, H. Nakai, T. Vreven, J. A. Montgomery, Jr., J. E. Peralta, F. Ogliaro, M. Bearpark, J. J. Heyd, E. Brothers, K. N. Kudin, V. N. Staroverov, R. Kobayashi, J. Normand, K. Raghavachari, A. Rendell, J. C. Burant, S. S. Iyengar, J. Tomasi, M. Cossi, N. Rega, J. M. Millam, M. Klene, J. E. Knox, J. B. Cross, V. Bakken, C. Adamo, J. Jaramillo, R. Gomperts, R. E. Stratmann, O. Yazyev, A. J. Austin, R. Cammi, C. Pomelli, J. W. Ochterski, R. L. Martin, K. Morokuma, V. G. Zakrzewski, G. A. Voth, P. Salvador, J. J. Dannenberg, S. Dapprich, A. D. Daniels, Ö. Farkas, J. B. Foresman, J. V. Ortiz, J. Cioslowski, and D. J. Fox, Gaussian, Inc., Wallingford CT, 2009.

[11] a) D. Jacquemin, E. A. Perpéte, I. Ciofini, C. Adamo, R. Valero, Y. Zhao, D. G. Truhlar, *J. Chem. Theory Comput.* **2010**, *6*, 2071; b) Y. Zhao, D. G. Truhlar, *Theor. Chem. Acc.* **2008**, *120*, 215; c) Y. Zhao, D. G. Truhlar, *J. Chem. Phys.* **2009**, *130*, 074103.

[12] a) J. Vura-Weis, M. A. Ratner, M. R. Wasielewski, *J. Am. Chem. Soc.* **2010**, *132*, 1738; b) N. Marom, A. Tkatchenko, M. Scheffler, L. Kronik, *J. Chem. Theory Comput.* **2010**, *6*, 81.

[13] N. L. Allinger, Y. H. Yuh, J. H. Lii, *J. Am. Chem. Soc.* **1989**, *111*, 8551.

[14] S. Plimpton, *J. Comp. Phys.* **1995**, *117*, 1.

[15] R. Cantrell, P. Clancy, *Surf. Sci.* **2008**, *602*, 3499.

[16] M. M. Francl, C. Carey, L. E. Chirlian, D. M. Gange, *J. Comput. Chem.* **1996**, *17*, 367.